

Determination of Residual Stresses in High Speed Milled Aluminium Alloys Using a Method of Indent Pairs

F.V. Díaz · R.E. Bolmaro · A.P.M. Guidobono ·
E.F. Girini

Received: 29 January 2009 / Accepted: 25 August 2009 / Published online: 16 September 2009
© Society for Experimental Mechanics 2009

Abstract An improved method of indent pairs is utilised to determine residual stresses in high speed milling specimens of AA 6082-T6 and AA 7075-T6 aluminium alloys. To carry out the measurement procedure, this approach does not need specific equipment but only requires a universal measuring machine and an oven. An indentation device is incorporated to the measuring machine, which allows reducing the absolute error of measurement to just ± 0.9 MPa. The geometry of the tool and cutting parameters are selected to evaluate the sensitivity of the method. The residual stress distributions generated by high speed milling are exhaustively evaluated taking into account orthogonal components of cutting speed and tangential force, which are parallel and perpendicular to feed direction.

Keywords Residual stresses · High speed milling · Aluminium alloys · Cutting parameters · Indentation methods

F.V. Díaz (✉)
Departamento de Ingeniería Electromecánica—Departamento
de Ingeniería Industrial, Facultad Regional Rafaela,
Universidad Tecnológica Nacional,
Bvd Roca 989,
2300 Rafaela, Argentina
e-mail: felipe.diaz@frra.utn.edu.ar

R.E. Bolmaro
Instituto de Física Rosario (CONICET—UNR),
Bvd 27 de Febrero 210 bis,
2000 Rosario, Argentina

A.P.M. Guidobono · E.F. Girini
División Metrología Dimensional,
Centro Regional Rosario (INTI),
2000 Rosario, Argentina

Nomenclature

A	elongation (%)
d	depth of cut (mm)
E	longitudinal elastic modulus (GPa)
f	feed rate (mm/rev)
F_{tx}	tangential force component at the x direction (N)
F_{ty}	tangential force component at the y direction (N)
HV0.5	Vickers micro-hardness (test load: 500 gf)
k_1, k_2	elastic constants
K	thermal conductivity (w/(m·K))
R_t	non-dimensional thermal number
S	specific heat capacity (J/(kg·K))
u	displacement component at the x direction (μm)
v	displacement component at the y direction (μm)
V	cutting speed (m/min)
V_x	cutting speed component at the x direction (m/min)
V_y	cutting speed component at the y direction (m/min)
X_b, X_a	distances between indents located at the x direction, before and after the stress-relieving, respectively (mm)
Y_b, Y_a	distances between indents located at the y direction, before and after the stress-relieving, respectively (mm)
α	clearance angle (deg)
β	fraction of energy from primary cutting zone to specimen surface
γ	rake angle (deg)
ε_x	deformation component at the x direction

ε_y	deformation component at the y direction
ν	Poisson's ratio
ρ	density (kg/m ³)
σ_x	residual stress component at the x direction (MPa)
σ_y	residual stress component at the y direction (MPa)
σ_u	ultimate tensile strength (UTS) (MPa)
$\sigma_{y0.2}$	yield strength (MPa)
ϕ	shear angle (deg)
χ	entrance angle (deg)
Δu	absolute error inherent to the u component (μm)
Δv	absolute error inherent to the v component (μm)
$\Delta X_b, \Delta X_a$	absolute errors inherent to the distances X_b and X_a , respectively
$\Delta Y_b, \Delta Y_a$	absolute errors inherent to the distances Y_b and Y_a , respectively
$\Delta \varepsilon_x$	absolute error inherent to the ε_x component
$\Delta \varepsilon_y$	absolute error inherent to the ε_y component
$\Delta \sigma_x$	absolute error inherent to the σ_x component (MPa)
$\Delta \sigma_y$	absolute error inherent to the σ_y component (MPa)
$\Delta \sigma_x^d$	variation in the σ_x component due to an increase in the d parameter (MPa)
$\Delta \sigma_y^d$	variation in the σ_y component due to an increase in the d parameter (MPa)
$\Delta \sigma_y^f$	variation in the σ_y component due to an increase in the f parameter (MPa)

Introduction

Residual stresses in a solid body are those self equilibrating stresses that exist without the application of external loads or constraints on its boundary. These stresses are developed when the solid body undergoes inhomogeneous plastic deformation and/or is exposed to a non-uniform temperature distribution [1, 2]. Residual stresses, which are difficult to measure and predict, should be added to the stresses generated by applied loads. Their measurement and prediction is important because of the undesirable effects they might generate. Tensile residual stresses can significantly reduce fatigue strength and also may induce stress corrosion cracking [3, 4]. On the other hand, compressive residual stresses would generate opposite effects. Furthermore, both tensile and compressive residual stresses may cause distortion and dimensional variation.

Measurement of residual deformations can be accomplished by means of a strain sensor, which is sensitive to

the changes generated on the surface of the evaluated component when stresses are relieved [5, 6]. Usually, the strain sensor is glued to the evaluated surface. The stress-release can be achieved by cutting and sectioning, trepanning and coring, or by drilling on the very region to be studied. The approaches based on the application of sensors have been used longer than any other technique. The more successful one is the hole-drilling method [7].

The displacements generated by stress-relieving can also be measured using coherent optics techniques [8]. Fringe patterns can be obtained by these non-contact techniques, from which residual displacements can be calculated. Their advantages include faster data collection, access to smaller regions and information of the displacement field corresponding to the measurement area. Moiré interferometry [9, 10], holographic interferometry [11, 12] and digital speckle pattern interferometry [13–15] have been successfully used in combination with the hole-drilling technique.

On the other hand, X-ray diffraction (XRD) strain measurement does not require a stress-relieving procedure. XRD techniques are able to measure the inter-planar distances of a metal or ceramic polycrystalline material [16, 17]. These inter-planar distances are indicative of the macrostrain undergone by the evaluated specimen. XRD is basically a non-destructive method for determining residual stresses in shallow surface layers. The neutron diffraction technique works in a similar way to the XRD but, because of neutrons penetration capabilities, residual stresses can be determined at larger depths [18]. Although other non-destructive techniques (e.g., ultrasonic, electromagnetic) have been developed for the same purposes, they still have to achieve wide acceptance as standardized methods of residual stress analysis [5].

Residual stresses can also be determined through instrumented indentation. Most approaches compare the contact depth or load-displacement curve of stressed and unstressed specimens, from which the residual stresses can be estimated [19–21]. Recently, an approach based on the change in spacing of indent pairs was developed [22]. The change in spacing occurs when residual stresses are relaxed through a thermal treatment. This method has the great advantage of being simple and inexpensive because it does not need specific equipment. For measuring the residual displacements, this approach only requires a universal measurement machine, a micro-hardness tester and an oven, which are commonly available in many workshops.

Machining is one of the most important manufacturing processes, and a constant search for cutting procedures, allowing diminishing costs of production, is currently underway. Costs could be further reduced by increasing the processing parameter values such as feed rate and cutting velocity [23]. If these increases are significant,

conventional machining is transformed into high-speed machining (HSM) [24]. This kind of machining has many advantages regarding conventional machining such as higher productivity, increased production flow time, reduced number of technological operations and longer service time of tools. Furthermore, HSM generates an equivalent or better surface finish, form, and size accuracy. However, high speed machined components can fail prematurely due to the development of residual stresses [25].

The purpose of this paper is to demonstrate the feasibility and sensitivity of an improved method of indent pairs for the evaluation of residual stress distributions generated by HSM. It must be noted that where the method of indent pairs was presented [22], the results were somehow preliminary, and therefore the method was not correctly validated. On the contrary, in this work an exhaustive analysis of measurement errors and a meticulous evaluation of different residual stress distributions help on the validation of the improved method. In the present paper, an indentation device was incorporated to the universal measurement machine, which allowed introducing elongated indents with great precision. From the shape and localization of these elongated indents, the absolute error of measurement could be reduced to just ± 0.9 MPa. Tests of high speed milling were performed in specimens of AA 6082-T6 and AA 7075-T6 aluminium alloys. The residual stresses were calculated from the measured displacements using a model for plane stress state [26]. The sensitivity of the method was assessed from a selection of process parameters that generated very weak residual stress distributions. The residual stress distributions were analysed taking into account orthogonal components of cutting speed, which are parallel and perpendicular to the feeding direction. This analysis showed which cutting force component is more important on residual stress introduction. Finally, the sensitivities of both machined alloys to develop residual stresses were also evaluated.

Residual Stress Determination

The technique used in this work to determine the residual stresses is based on the change in distance between pairs of micro-hardness indents. As mentioned above, this change occurs when the evaluated specimen is heat treated for releasing the residual stresses. The measurement procedure is detailed in ref. [22]. Briefly, this procedure is as follows. First, an indent distribution is introduced on the specimen surface using a micro-hardness tester. Then, before and after the stress-relieving treatment, the distances between indent pairs are measured using a universal measuring

machine. It must be noted that this method allows to determine all components of the in-plane residual stress. For measurement of the through-thickness residual stress distribution, progressive removal of uniform layers from the specimen surface by chemical etching should be implemented. However, in out-of-plane direction, residual stresses are usually difficult to measure in thin layers of deposited or affected material, even by volumetric techniques like neutron diffraction [5].

In this paper, the measurement procedure does not require a micro-hardness tester. The indent distribution was introduced using a mechanical device mounted on the measuring machine. Figure 1(a) shows a front view of the device. The body of the device is made up of a system of thin elastic plates that enables to regulate the indentation load. This device is attached to an electronic sensor, which allows

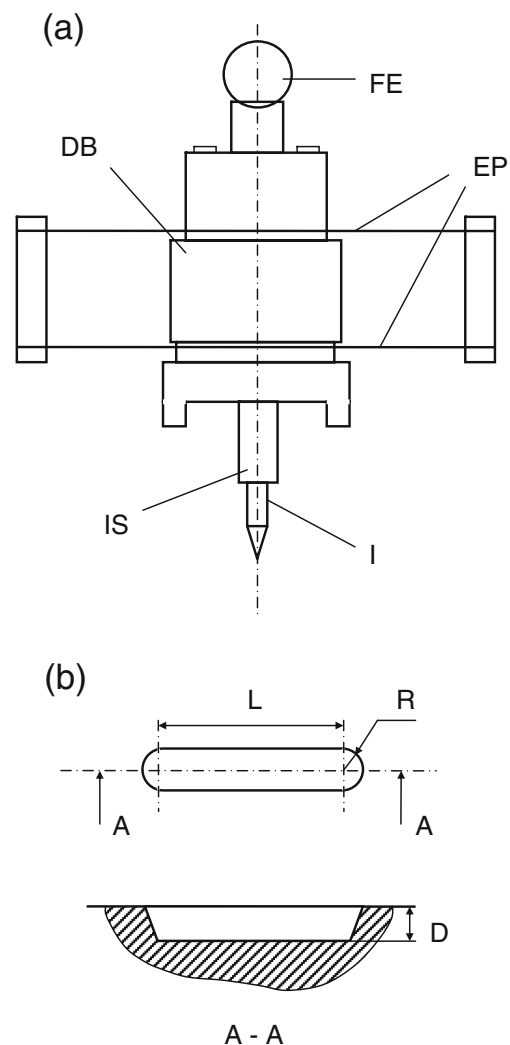


Fig. 1 Scheme of indentation: (a) front view of the indentation device: (FE) fixation sphere, (DB) device body, (EP) elastic plates, (I) indentator, (IS) indentator support; (b) geometry of an elongated indent: (L) indent length, (R) end radius, (D) indent depth

calibrating the depth of the indent with high accuracy. Using this mechanical device it is possible to introduce elongated indents. Figure 1(b) shows the geometry of an elongated indent.

The orthogonal components of the in-plane residual stress (σ_x , σ_y) can be determined from an indent distribution as shown in Fig. 2. The distance between pairs of elongated indents (e.g., A–B, C–D) will diminish if the released residual stresses are of tensile character. On the other hand, this distance will increase in the case of relieving compressive residual stresses. Therefore, from this indent distribution, the residual displacements can be expressed as

$$u = X_b - X_a$$

$$v = Y_b - Y_a \quad (1)$$

where X_b and X_a are the distances between the indents A and B, before and after the stress-relieving procedure, respectively. On the other hand, Y_b and Y_a correspond to the spacing between indents C and D, before and after the same thermal treatment, respectively. Then, the residual deformations can be determined by

$$\varepsilon_x = \frac{X_b}{X_a} - 1$$

$$\varepsilon_y = \frac{Y_b}{Y_a} - 1 \quad (2)$$

Finally, assuming a plane stress state on the surface of the specimen, the in-plane residual stress orthogonal components can be expressed for isotropic, linear elastic materials as [26]

$$\sigma_x = k_1 \cdot \varepsilon_x + k_2 \cdot \varepsilon_y$$

$$\sigma_y = k_1 \cdot \varepsilon_y + k_2 \cdot \varepsilon_x \quad (3)$$

where $k_1 = E/(1 - \nu^2)$, $k_2 = \nu \cdot k_1$, E is the longitudinal elastic modulus and ν is the Poisson's ratio.

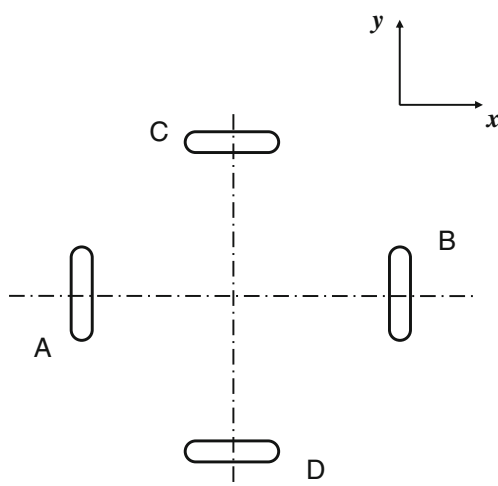


Fig. 2 Distribution of elongated indents for orthogonal measurement

Error Analysis

The absolute error on the measurement of the distance between elongated indents was obtained. Besides, this error was compared to the absolute error inherent to the measurement of the distance between pyramidal indents, which were introduced using a micro-hardness tester (Shimadzu HMV-2). Figure 3 shows both types of indents, which were generated on the surface of different machined aluminium alloy samples. Although local residual stress fields are introduced by indentation, the errors generated by those fields can be minimized by a proper separation of the evaluated indents. In our case, the nominal distance between each indent pair was 28 mm. The indent coordinates were optically measured using a precision microscope incorporating the universal measurement machine (GSIP MU-314). From taking six measurements for each coordinate and considering the systematic error, the maximum absolute errors corresponding to the distances between pyramidal and elongated indents were $\pm 0.2 \mu\text{m}$ and $\pm 0.16 \mu\text{m}$, respectively.

The measurement procedure includes the repositioning of the specimen after the stress-relieving treatment. Therefore, the error corresponding to the distance between indents after the thermal treatment must take into account the repositioning uncertainty. This uncertainty was obtained for both types of indents from different repositioning sequences. Following the same procedure, that is to say, from taking six measurements for each coordinate and considering both the systematic error and the repositioning uncertainty, the maximum absolute errors corresponding to pyramidal and elongated indent distances were $\pm 1.51 \mu\text{m}$

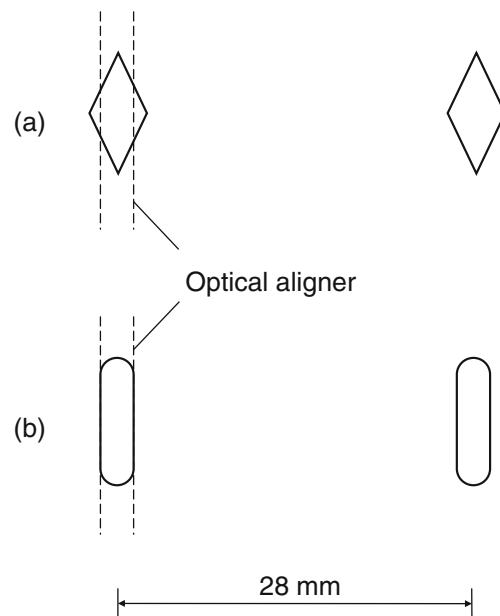


Fig. 3 (a) Pyramidal and (b) elongated indents

and $\pm 0.26 \mu\text{m}$, respectively. This important difference is due to the final alignment of the repositioning procedure. The alignment of pyramidal and elongated indents is shown in Fig. 3. As it can be seen, the alignment of pyramidal indent edges is quite difficult, while the great straightness of the edges of the elongated indents helps us to carry out an optimum alignment.

Then, the absolute errors corresponding to the residual displacements can be obtained from the distance measurement errors using [27]

$$\begin{aligned}\Delta u &= \sqrt{\Delta X_b^2 + \Delta X_a^2} \\ \Delta v &= \sqrt{\Delta Y_b^2 + \Delta Y_a^2}\end{aligned}\quad (4)$$

where ΔX_b and ΔX_a are the absolute errors corresponding to the distances between indents located at the x direction (Fig. 2), before and after the repositioning, respectively. On the other hand, ΔY_b and ΔY_a are the absolute errors corresponding to the distances between indents situated at the y direction, also before and after the repositioning, respectively. Because the residual deformations (ε_x , ε_y) are calculated from the distances between indents, the absolute errors can be obtained using [27]

$$\begin{aligned}\Delta \varepsilon_x &= \sqrt{\left(\frac{\Delta X_b}{X_a}\right)^2 + \left(\frac{\Delta X_a}{X_b}\right)^2} \cdot X_b^2 \\ \Delta \varepsilon_y &= \sqrt{\left(\frac{\Delta Y_b}{Y_a}\right)^2 + \left(\frac{\Delta Y_a}{Y_b}\right)^2} \cdot Y_b^2\end{aligned}\quad (5)$$

Finally, the absolute errors corresponding to the residual stresses can be obtained from the errors corresponding to the residual deformations using [27]

$$\begin{aligned}\Delta \sigma_x &= \sqrt{k_1^2 \cdot \Delta \varepsilon_x^2 + k_2^2 \cdot \Delta \varepsilon_y^2} \\ \Delta \sigma_y &= \sqrt{k_1^2 \cdot \Delta \varepsilon_y^2 + k_2^2 \cdot \Delta \varepsilon_x^2}\end{aligned}\quad (6)$$

Table 1 shows the absolute errors corresponding to the displacements, deformations and stresses, which were calculated using equations (4–6). As it can be seen, through the introduction of elongated indents, the absolute errors can be substantially reduced.

Table 1 Comparison of absolute errors

Indentation	Absolute error		
	Displacements u, v (μm)	Deformations $\varepsilon_x, \varepsilon_y$ (%)	Stresses σ_x, σ_y (MPa)
Elongated	0.3	0.001	0.9
Pyramidal	1.5	0.005	4.5

Materials and Procedures

The experimental investigations were performed in two rolling products which can be considered to have middle and high mechanical resistance (yield and ultimate tensile strength). The AA 6082-T6 and AA 7075-T6 aluminium alloys were selected because they have good machinability (curled or easily broken chips and good to excellent finish). It must be noted that AA 6082-T6 is a relatively new alloy, which is used in structural applications in the marine and transportation industries as well as for machined precision parts in the automotive industry. On the other hand, AA 7075-T6 is a structural alloy widely used for aircraft, aerospace and defense applications due to its high mechanical resistance/weight ratio. The chemical compositions and, elastic and mechanical properties of these alloys are reported in Tables 2 and 3, respectively.

The dimensions of the tested specimens were $110 \times 40 \times 4 \text{ mm}^3$. Before milling tests, each specimen was subject to a simple stress-relieving procedure in an oven, using an annealing temperature and time of 573 K and 80 min, respectively. In order to evaluate the method sensitivity, the process parameters and tool geometry were selected to induce low residual stress states. High speed milling tests were performed using a face mill of 63 mm in diameter. Five tungsten carbide inserts (Palbit SEHT 1204 AFFN-AL SM10) were incorporated to the face mill. The geometry of these inserts was specially designed for use with aluminium alloys. Edges are very keen and cutting faces are highly polished so as to remove swarf efficiently and prevent it from bonding to the insert. The face mill was attached to the spindle of a Clever CMM-100 vertical CNC milling machine, which is a rigid machine tool with powerful axis drives and large precision ball screws. Figure 4 shows an upper view of the system specimen-tool. The cutting conditions and the tool geometry are given in Table 4. All of the HSM tests were carried out without cutting fluid.

For each specimen, the following measurement procedure was carried out. First, a distribution of elongated indents on the machined surface was introduced, which allowed to calculate the stress components in different points corresponding to both symmetry axes of this surface. Afterwards, the indent coordinates were optically measured using the universal measurement machine mentioned above. Then, in order to remove the specimen ends, which were not machined (Fig. 4), an electro-discharge cutting was carried out. An annealing treatment at 573 K during 80 min, to relieve the machined surface stresses, was performed after the cutting. Then, the specimen was repositioned and optically aligned. Finally, the indent coordinates were again measured following the same procedure. Both measurements, before and after the stress-

Table 2 Chemical composition of the investigated aluminium alloys

Alloy	Chemical composition (wt %)							
	Zn	Mg	Cu	Fe	Si	Cr	Mn	Al
6082-T6	0.2	0.9	0.15	0.5	0.9	0.22	0.6	balance
7075-T6	5.6	2.52	1.72	0.32	0.2	0.17	0.16	balance

relieving treatment, were performed in the temperature range of $20 \pm 0.2^\circ\text{C}$.

Results and Discussion

The orthogonal components of the in-plane residual stress (σ_x , σ_y) were evaluated along both symmetry axes of the machined surfaces. Figure 5(a) shows the residual stress component σ_x obtained for different points of the axis $y=0$ when the cutting speed and feed rate are fixed. It must be noted that the direction of this stress component is perpendicular to the feeding direction. For alloy 6082-T6, stresses are larger when the depth of cut is increased. Moreover, both distributions have the same shape. The minimal values are located at the centre of the axis and the maximum values are situated at the axis ends. On the other hand, the stress distribution shapes of the alloy 7075-T6 are similar to those corresponding to alloy 6082-T6 but the stress values are near zero. Besides, the difference between both distributions is smaller than that corresponding to alloy 6082-T6. Figure 5(b) shows the same stress component σ_x but along the axis $x=0$. The stress distributions of the alloy 6082-T6 are negative and almost constant. Moreover, the stress level diminishes when the depth of cut is increased. In addition, the response of the alloy 7075-T6 is shown in the same graph. In this case, the stress distributions are also negative and almost constant but the stress levels are near zero.

Figure 6(a) shows the distributions of the other stress component σ_y , along the axis $y=0$. For alloy 6082-T6, the increase in depth of cut does not generate changes in the stress distribution shape. The same stress distribution shapes are obtained for alloy 7075-T6 but the difference between both distributions is smaller than that corresponding to alloy 6082-T6. Besides, the latter generates more compressive stresses. Fig. 6(b) shows how the same component σ_y is distributed along the axis $x=0$. As it can be seen, the stress

levels are similar to those shown in Fig. 6(a) but all distributions are constant.

Figure 7 shows the distributions of the same stress component σ_y , obtained along both symmetry axes when the feed rate is increased. Figure 7(a) shows how both alloys are stressed when this process parameter is $f=0.1$ mm/rev. Both distributions have similar shapes. As the distributions shown in Figs. 5(a) and 6(a), the minimal values are located at the centre of the axis, and the gradients from the centre to the left end of the axis are higher than those from the centre to the right end of the axis. Figure 7(b) shows the stress distributions generated when the feed rate is $f=0.2$ mm/rev. Although the stress distribution shapes do not change, the gradients are higher than those shown in Fig. 7(a). On the other hand, the distributions obtained for the same stress component σ_y , but along the other symmetry axis are shown in Figs. 7(c) and (d). The distributions corresponding to both alloys are similar and the stress level difference is smaller when the feed rate is $f=0.1$ mm/rev [Fig. 7(c)]. As expected, the shapes of the distributions do not change and the stresses are more compressive when the process parameter is $f=0.2$ mm/rev [Fig. 7(d)].

For the investigated cutting conditions, the obtained residual stresses are compressive and very low. Along the axis $y=0$, which is perpendicular to the feed direction, the distributions of both stress components have similar shapes, with the minimum value situated at the axis centre, and gradients from the centre to the axis ends showing a small asymmetry. Along the axis $x=0$, which is parallel to the feed direction, the distributions are constant or almost constant.

In each machining test, the proper tool angles, tool finishing, depth of cut, feed and cutting speeds generated stable cutting conditions corresponding to low cutting forces and good chip formation (very small broken chips). Due to the important role played by high cutting speed in the generation of stable cutting conditions, the stress distribution shapes were compared to those corresponding

Table 3 Elastic and mechanical properties of the investigated aluminium alloys

Alloy	Properties					
	σ_u (MPa)	$\sigma_{y0.2}$ (MPa)	A (%)	HV0.5	E (GPa)	ν
6082-T6	341	314	11	108	70	0.33
7075-T6	564	506	11	186	70	0.33

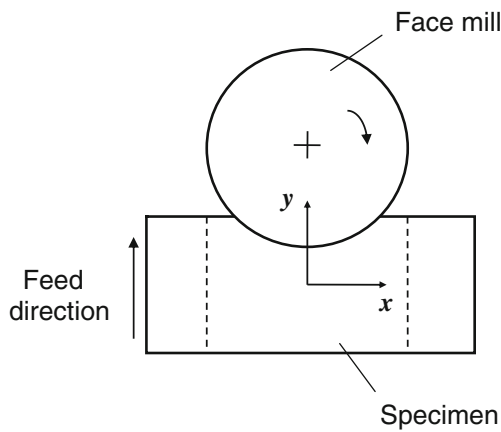


Fig. 4 Diagram of the specimen-tool system

to the orthogonal component distributions of cutting speed (V_x, V_y) along the same axes. Figure 8 shows the distributions of these components. Along the axis $y=0$, the V_x component shows a narrow variation range and its sign does not change, and the V_y component shows a broad variation range and its sign changes [Fig. 8(a)]. On the other hand, along the axis $x=0$, the V_x component is constant and the V_y component is zero [Fig. 8(b)]. It is obvious that, along this axis $x=0$, the V_y component cannot influence the generation of stresses, and besides, the distribution of the V_x component is similar to the distributions of both stress components along the same axis [Figs. 5(b), 6(b), 7(c) and (d)]. In addition, along the axis $y=0$, the V_y component could influence the generation of stresses but only the distribution of the V_x component is similar to the distributions of both stress components along the same axis [Figs. 5(a), 6(a), 7(a) and (b)].

This brief analysis indicates that cutting tangential force component, associated to the V_x component, would govern the surface residual stresses that generate the local plastic deformation. Figure 9 shows the distribution of the tangential force component F_{tx} along both symmetry axes when the values of depth of cut and feed speed are larger. It must be noted that for another cutting parameter combinations, also evaluated in this work, the distribution shapes corresponding to this component do not change. This force component was calculated from the material removal rate, the specific power and the instantaneous chip thickness [23]. As expected, the values of the F_{tx} component are low. When cutting forces and surface heating are relatively low, the compaction of surface layers is expected to be very

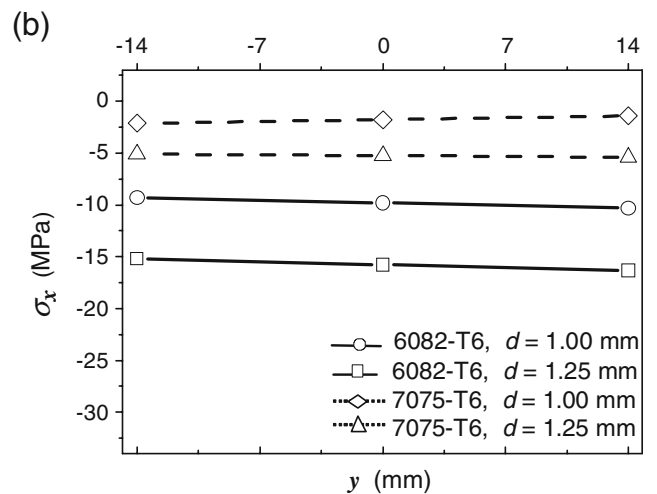
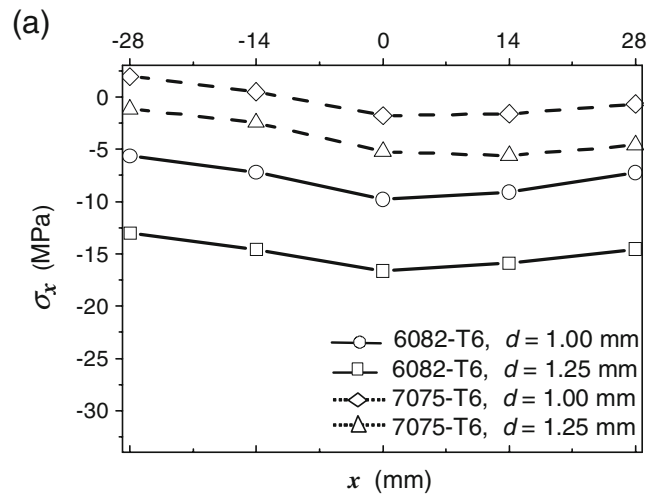


Fig. 5 Distributions of the stress component σ_x along the axes (a) $y=0$ and (b) $x=0$ (cutting speed: $V=1000$ m/min, feed rate: $f=0.2$ mm/rev)

smooth, and then, introduced residual stresses will be compressive and low [25]. On the contrary, when forces and surface temperatures increase, the thermal expansion of the surface is constrained by the surrounding region, leading to plastic deformation compression of the heated area from which tensile residual stresses are introduced.

The general shape of the residual stress distributions would respond to the mechanical effects generated by the F_{tx} component and, in addition, the final level these distributions reach could be due to thermal effects on specimen surfaces. However, along the axis $x=0$, the F_{tx} component distributions are symmetrical and, as mentioned

Table 4 Cutting conditions and tool geometry

Rake angle γ (°)	Clearance angle α (°)	Entrance angle χ (°)	Cutting speed V (m/min)	Feed rate f (mm/rev)	Depth of cut d (mm)
45	7	45	1000	0.1–0.2	1.00–1.25

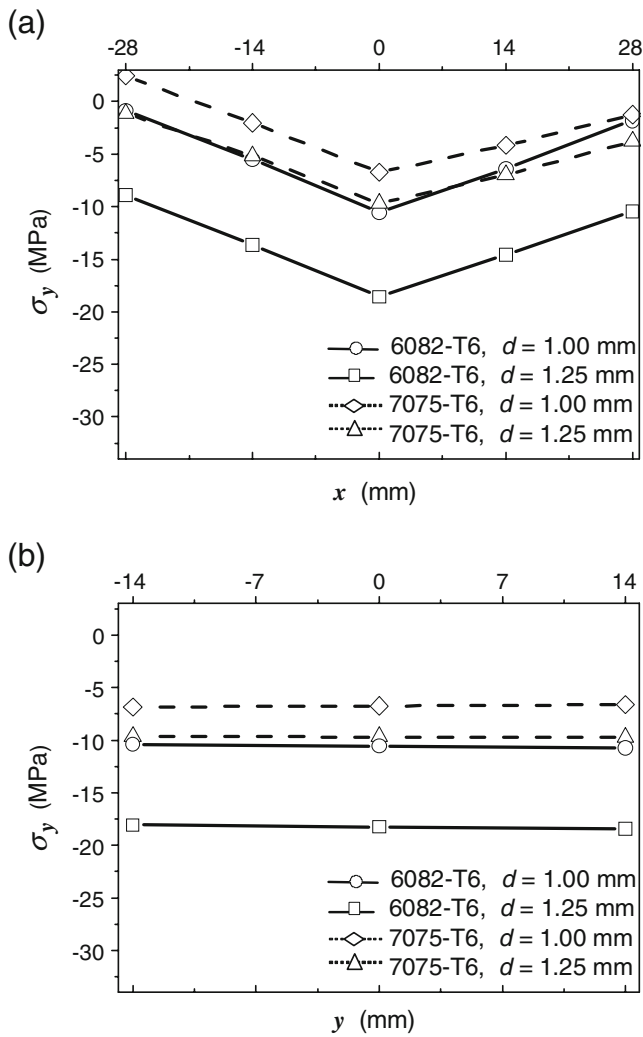


Fig. 6 Distributions of the stress component σ_y along the axes (a) $y=0$ and (b) $x=0$ (cutting speed: $V=1000$ m/min, feed rate: $f=0.2$ mm/rev)

above, the stress distributions show a small asymmetry: the gradients from the axis centre to the axis ends are different. This asymmetry can be explained as follows. For $x>0$, the V_y component and feed rate have opposite direction (conventional cutting), and for $x<0$, this component and feed rate have the same direction (climb cutting). The gradients from the centre to the axis right end ($x>0$) are slightly lower because conventional cutting generates slightly more compressive stresses than climb cutting. It occurs that conventional cutting is so light at the beginning that each insert slides on specimen surface until sufficient pressure is built up and it begins to cut. This introduces a small additional increase in local plastic deformation of machined surface, which does not occur in the case of climb cutting [23].

Although both alloys generated the same residual stress patterns when they were machined by the same process parameters, it can be observed that alloy 6082-T6 is more

sensitive to the changes in process parameters than alloy 7075-T6. Table 5 reports the stress increments generated at the barycentre of the machined surfaces due to the variation of the process parameters. It must be noted that all increments are negative. As it can be seen, the increase in depth of cut (25 %) leads to similar changes in both stress components. Furthermore, for the σ_y component, this increase in depth of cut leads to a bigger change than the increase in feed rate (100 %). From this Table, it is possible to express the relationships between the increments corresponding to both alloys. The relationship between increments of σ_x

$$\frac{\Delta\sigma_{x6082}^d}{\Delta\sigma_{x7075}^d} \approx 2$$

would quantify the sensitivity difference to the change in the d parameter when the stress component perpendicular to the feed direction is evaluated. Moreover, the relationships between increments of σ_y

$$\frac{\Delta\sigma_{y6082}^d}{\Delta\sigma_{y7075}^d} \approx \frac{\Delta\sigma_{y6082}^f}{\Delta\sigma_{y7075}^f} \approx 2.7$$

would indicate that both alloys maintain a strict difference of sensitivity to the proposed modifications in both process parameters when the stress component parallel to feed direction is evaluated.

The difference on sensibility between both alloys could be explained through the evaluation of thermal effects generated in the cutting zone. In first place, a big part of the heat generated in the tool-chip interface would be evacuated by chips at high speed. Secondly, the thermal flow from the cutting primary zone [23] to the specimen surface could establish the final level reached by each stress distribution. The fraction of the energy generated in the cutting primary zone that enters in the machined surface can be expressed as [28]

$$\beta = 0.5 - 0.35 \cdot \log(R_t \cdot \tan \phi) \quad \text{for } 0.04 \leq R_t \cdot \tan \phi \leq 10.0$$

$$\beta = 0.3 - 0.15 \cdot \log(R_t \cdot \tan \phi) \quad \text{for } R_t \cdot \tan \phi > 10.0$$

(7)

where ϕ is the shear angle, $R_t = \rho \cdot S \cdot V \cdot d / K$, ρ is the density, S is the specific heat capacity and K is the thermal conductivity of the machined material. For the same cutting conditions, it is possible to express the relationship

$$\frac{R_{t6082}}{R_{t7075}} \approx 0.7$$

which indicates that the fraction of thermal energy β will always be higher for alloy 6082-T6, for similar shear angles for both alloys. The value obtained by this relationship

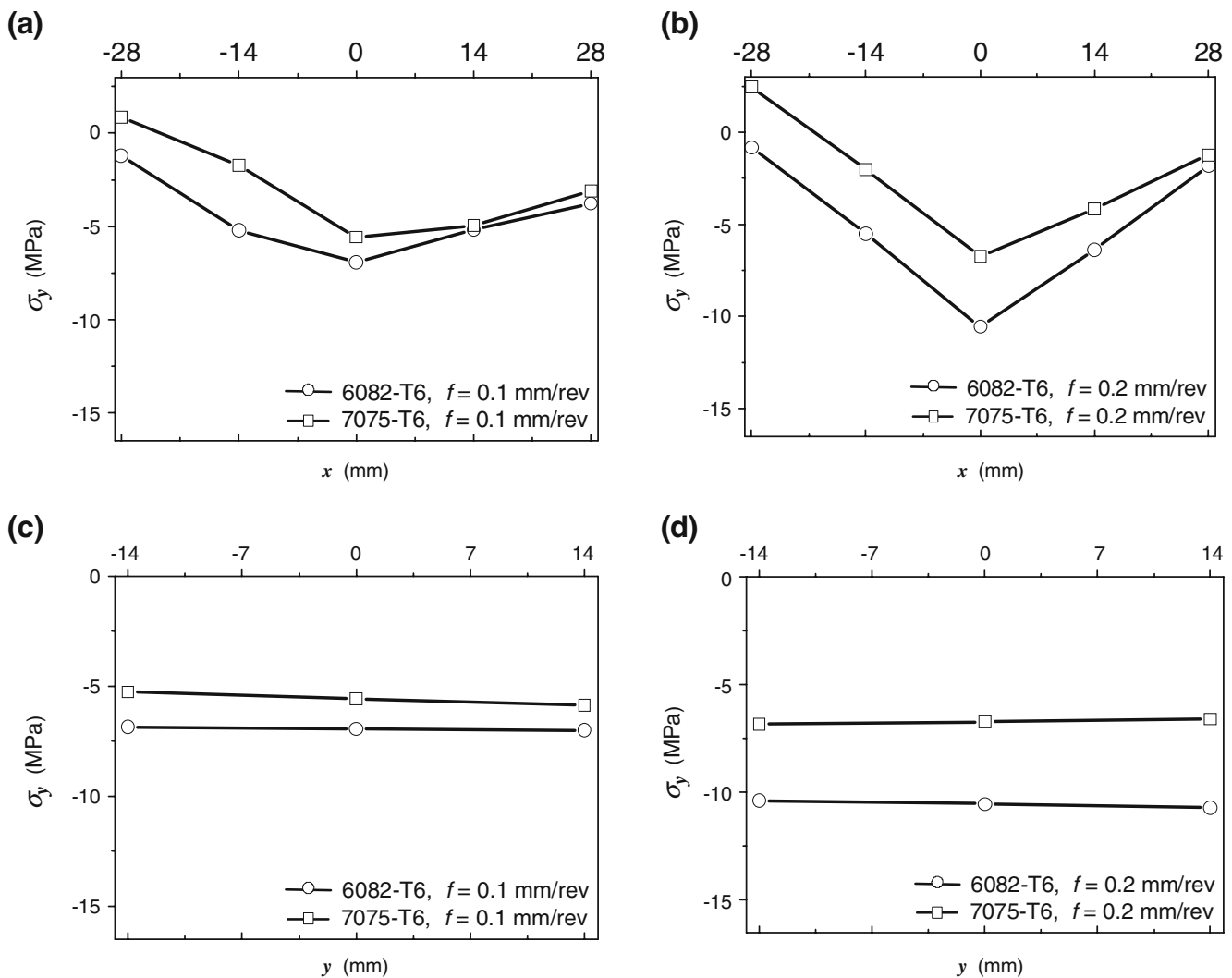


Fig. 7 Distributions of the stress component σ_y along the axes $y=0$ and $x=0$ (cutting speed: $V=1000$ m/min, depth of cut: $d=1.00$ mm, feed rate: (a) and (c) $f=0.1$ mm/rev, (b) and (d) $f=0.2$ mm/rev)

basically responds to the difference on thermal conductivity between both alloys ($K_{6082}/K_{7075} = 1.3$). In addition, both density and specific heat capacity are slightly higher for alloy 7075-T6.

On the other hand, the machinability of both alloys is not similar. Alloy 6082-T6 is more difficult to machine because the magnesium it contains is essentially tied up with silicon to form hard Mg_2Si particles [29]. The machinability difference between both alloys could compensate the small difference in cutting forces (higher for alloy 7075-T6), and then, it is possible to expect the thermal energy in the cutting primary zone to be similar for both alloys. Based on this hypothesis and the values adopted by the fraction of thermal energy β , the specimen surface temperature for alloy 6082-T6 will be higher than for alloy 7075-T6 when the same process parameters are selected. This implicates that for each increase in depth of cut or feed speed, the surface temperature augmentation

for alloy 6082-T6 will be higher and therefore, the increase in compressive residual stress will also be higher [25]. Finally, the observed strict relationships between residual stress increments would respond to strict relationships between surface temperatures.

Conclusions

A method of indent pairs has been improved to reduce the magnitude of the absolute measurement error inherent to the residual stress determination on the surface of machined samples. An indentation device was specially integrated to the universal measuring machine in order to introduce elongated indents with great precision. From the shape of this type of indent, it was possible to diminish the uncertainty inherent to the sample repositioning from ± 1.5 μm to ± 0.2 μm , and then, the

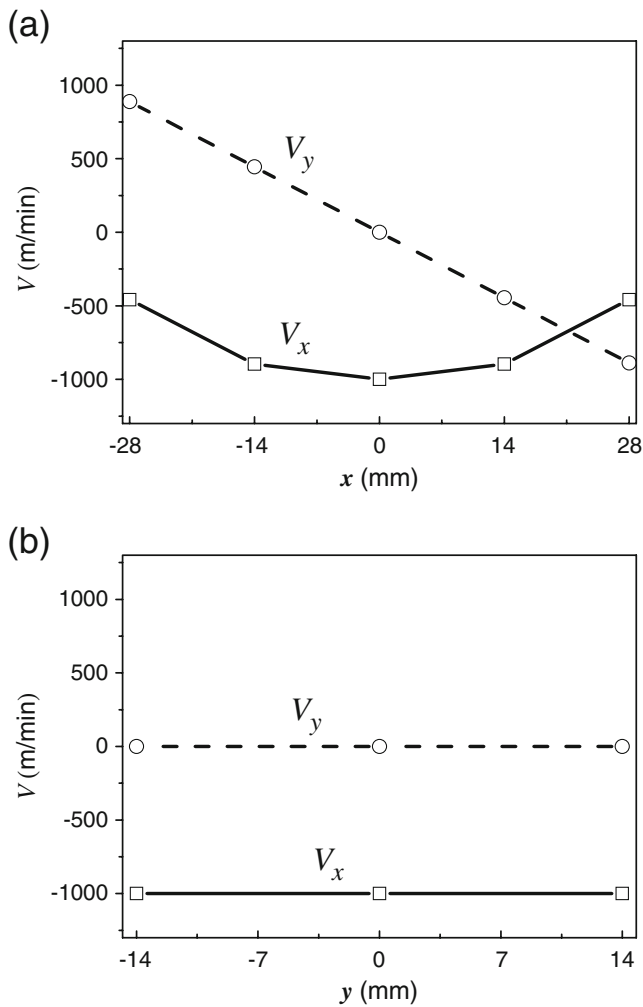


Fig. 8 Components of the cutting speed along the axes (a) $y=0$ and (b) $x=0$

measurement error from ± 4.5 MPa to ± 0.9 MPa. The utilization of the indentation device allowed reducing and optimizing the equipment for residual stress determination because only a universal measuring machine and an oven were used. The feasibility and sensitivity of this approach has been proved through the evaluation of residual stress distributions generated by high speed milling, which showed to be compressive and very low. The shapes of the obtained stress distributions were similar for both analysed aluminium alloys. These shapes (or patterns) may respond to mechanical effects generated by the F_{tx} component of the cutting tangential force, which is perpendicular to the feed direction. The maximum stress levels depended on the alloy type. Alloy 6082-T6 showed to be more sensitive to the modifications in process parameters than alloy 7075-T6. The sensitivity difference between both alloys, which showed to be similar for both analysed in-plane stress components, may be caused by small differences in the thermal flow from the primary cutting zone to the specimen surface.

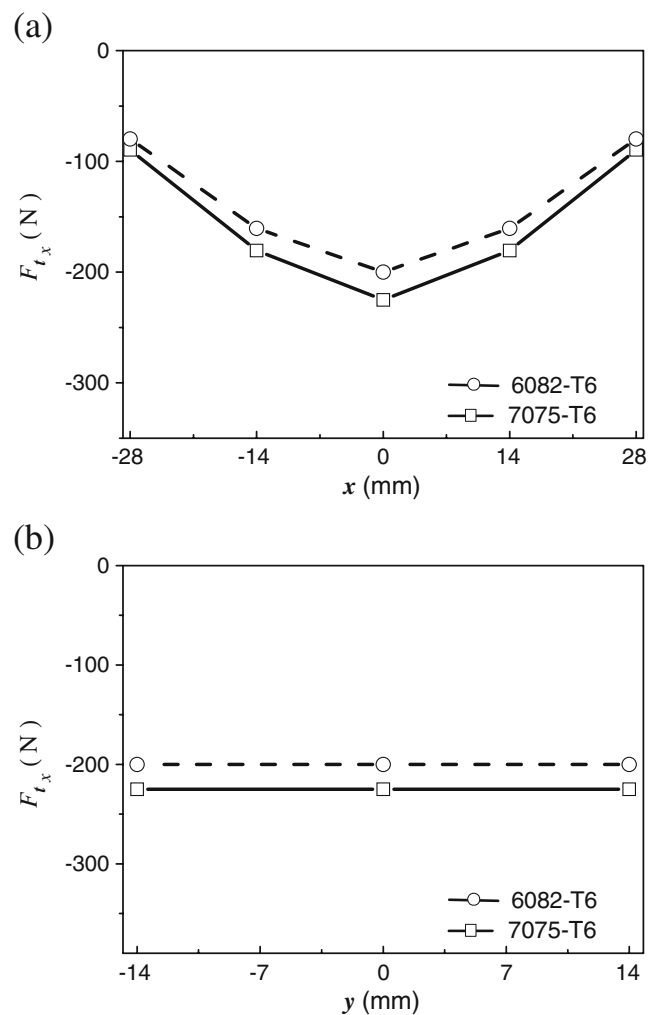


Fig. 9 Tangential force component F_{tx} along the axes (a) $y=0$ and (b) $x=0$ (cutting speed: $V=1000$ m/min, depth of cut: $d=1.25$ mm, feed rate: $f=0.2$ mm/rev)

Acknowledgments The authors wish to express their sincere thanks to Eduardo Cravero and Silvio Acosta for their assistance during HSM test phase. This work was supported by the Departamento de Ingeniería Electromecánica and the Departamento de Ingeniería Industrial, Facultad Regional Rafaela, Universidad Tecnológica Nacional.

Table 5 Stress increments at the barycentre of the machined surfaces

Alloy	Stress increments (MPa)		
	$\Delta\sigma_x^d$	$\Delta\sigma_y^d$	$\Delta\sigma_y^f$
6082-T6	- 6.84	- 8.00	- 3.61
7075-T6	- 3.48	- 2.96	- 1.37



References

1. Lu J (ed) (1996) Handbook of measurement of residual stresses, SEM. Fairmont, Lilburn
2. Rowlands RE (1987) Residual stresses. In: Kobayashi AS (ed) Handbook on experimental mechanics. Prentice-Hall, New Jersey, pp 768–813
3. Schwach DW, Guo YB (2006) A fundamental study on the impact of surface integrity by hard turning on rolling contact fatigue. *Int J Fatigue* 28:1838–1844
4. Toribio J (1998) Residual stress effects in stress-corrosion cracking. *J Mater Eng Perform* 7:173–182
5. Withers PJ, Bhadeshia HK (2001) Residual stress. Part 1—Measurement techniques. *Mater Sci Technol* 17:355–365
6. Guo YB, Ammula SC, Barkey ME (2006) A wet etching method coupled with finite element analysis based compliance function to determine residual stress by high speed milling. *J Manuf Sci Eng* 128:792–801
7. Rendler NJ, Vigness I (1966) Hole-drilling strain-gage method of measuring residual stresses. *Exp Mech* 6:577–586
8. Furgiuele FM, Pagnotta L, Poggialini A (1991) Measuring residual stresses by hole drilling and coherent optics techniques: a numerical calibration. *J Eng Mater Technol* 113:41–50
9. McDonach A, McKelvie J, MacKenzie PM et al (1983) Improved moiré interferometry and applications in fracture mechanics, residual stress and damaged composites. *Exp Tech* 7:20–24
10. Nicoletto G (1991) Moiré interferometry determination of residual stresses in the presence of gradients. *Exp Mech* 31:252–256
11. Antonov AA (1983) Inspecting the level of residual stresses in welded joints by laser interferometry. *Weld Prod* 30:29–31
12. Nelson DV, McCrickerd JT (1986) Residual stress determination through combined use of holographic interferometry and blind hole drilling. *Exp Mech* 26:371–378
13. Zhang J (1998) Two-dimensional in-plane electronic speckle pattern interferometer and its application to residual stress determination. *Opt Eng* 37:2402–2409
14. Díaz FV, Kaufmann GH, Galizzi GE (2000) Determination of residual stresses by hole drilling and digital speckle pattern interferometry with data automatic analysis. *Opt Lasers Eng* 33:39–48
15. Díaz FV, Kaufmann GH, Möller O (2001) Residual-stress determination using blind-hole drilling and digital speckle pattern interferometry with automated data processing. *Exp Mech* 41:319–323
16. Noyan IC, Cohen JB (1987) Residual stress measurement by diffraction and interpretation, Materials Research and Engineering. Springer Verlag, Berlin
17. Prevéy PS (1987) X-ray diffraction residual stress techniques. In: Metals Handbook, American Society for Metals, pp 380–401
18. Allen AJ, Hutchings MT, Windsor CG et al (1985) Neutron diffraction methods for the study of residual stress fields. *Adv Phys* 34:445–473
19. Suresh S, Giannakopoulos AE (1998) A new method for estimating residual stresses by instrumented sharp indentation. *Acta Mater* 46:5755–5767
20. Swadener JG, Taljat B, Pharr GM (2001) Measurement of residual stress by load and depth sensing indentation with spherical indenters. *J Mater Res* 16:2091–2102
21. Zhao M, Chen X, Yan J et al (2006) Determination of uniaxial residual stress and mechanical properties by instrumented indentation. *Acta Mater* 54:2823–2832
22. Wyatt JE, Berry JT (2006) A new technique for the determination of superficial residual stresses associated with machining and other manufacturing processes. *J Mater Proc Tech* 171:132–140
23. Trent EM (1991) Metal cutting. Butterworth/Heinemann, London
24. Schulz H (1996) High speed machining. Carl Hanser, Munich
25. Mantle AL, Aspinwall DK (2001) Surface integrity of a high speed milled gamma titanium aluminide. *J Mater Proc Tech* 118:143–150
26. Timoshenko SP, Goodier JN (1970) Theory of elasticity, 3rd edn. McGraw-Hill, New York
27. Bevington PR, Robinson DK (2002) Data reduction and error analysis for the physical sciences. McGraw-Hill, New York
28. Özel T, Zeren E (2004) Determination of flow material stress and friction for FEA of machining using orthogonal cutting tests. *J Mater Proc Tech* 153:1019–1025
29. Kamiya M, Yakou T (2008) Role of second-phase particles in chip breakability in aluminium alloys. *Int J Mach Tools Manuf* 48:688–697